

Draft

GIC–Related Observations During the May 2024 Geomagnetic Storm in the United States

L. A. Wilkerson¹, R. S. Weigel¹, D. Thomas¹, D. Bor¹, E. J. Oughton¹, C. T.
Gaunt², C. C. Balch³, M. J. Wiltberger⁴, and A. Pulkkinen⁵

¹Space Weather Lab, George Mason University, Fairfax, VA

²University of Cape Town, Cape Town, ZA

³NOAA/SWPC, Boulder, CO

⁴NCAR/HAO, Boulder, CO

⁵NASA/GSFC, Greenbelt, MD

Abstract

The May 2024 geomagnetic storm was one of the most severe in the past twenty years. Understanding how large geomagnetic disturbances (GMDs) impact geomagnetically induced currents (GICs) within power grid networks is key to ensuring their resilience. We have assembled and synthesized a large and diverse set of GMD-related data, compared model predictions with measurements, and identified empirical relationships for GICs in the contiguous United States for this storm.

Measurement data include GIC data from 47 sites and magnetometer data from 17 magnetometer sites. Model data include computed GIC by the Tennessee Valley Authority (TVA) power system operators at four sites, GIC computed using a reference model at 47 sites, ΔB at 12 magnetometer sites from the Multiscale Atmosphere-Geospace Environment Model (MAGE), Space Weather Modeling Framework (SWMF), and Open Geospace General Circulation Model (OpenGGCM) global magnetosphere models, and β scaling factors derived from magnetotelluric (MT) transfer functions at $\sim 5,000$ MT sites.

GIC measured and modeled by TVA had a correlation coefficient > 0.8 and a prediction efficiency between 0.4 and 0.7. The horizontal magnetic field perturbation from a baseline, ΔB_H , predicted by MAGE, SWMF, and OpenGGCM had a correlation that ranged from 0.4 to 0.6. Two empirical relationships were considered: (1) how the correlation between measured GIC site pairs depended on differences in site separation distance, β scaling factor, and latitude; and (2) a regression model that predicts the standard deviation and maximum GIC magnitude at each site given inputs of site latitude and β .

1 Introduction

In May 2024, NOAA Active Region 13664 triggered a geomagnetic storm (which has been referred to as the “Gannon” and “Mother’s Day”), which was the most intense geomagnetic storm in over two decades (Kruparova et al. (2024); Tulasi Ram et al. (2024); Kwak et al. (2024)).

Between 7–11 May 2024, NASA reported observing multiple strong solar flares – eight of which were X-class – and at least seven coronal mass ejections (CMEs) (Johnson-Groh, 2024). NOAA’s Space Weather Prediction Center (SWPC) reported that the first

CME reached Earth on May 10, resulting in a geomagnetic storm that reached a rating of G5 – a level that had not occurred since October 2003 (SWPC, 2024a). The storm had the largest disturbance storm index (D_{st}) magnitude since March 1989 and the largest A_p index recorded of any modern solar event (i.e., since the Carrington Event of September 1859) (SWPC, 2024b). On 11 May, the daily A_p -index was 273 nT and D_{st} was -292 nT, the largest single-day magnitudes recorded in 22 years (Mlynczak et al., 2024).

During the storm, aurora extended to mid-latitudes, with the southern aurora reaching the southern parts of Africa and South America (Karan et al., 2024), and the northern aurora was visible across much of the United States (SWPC, 2024a). The storm has also been associated with interruptions to flight and satellite operations, particularly those in low Earth orbit (LEO) (Parker & Linares, 2024). In Mexico, GIC intensities of ~ 30 A were observed at low-latitude 400 kV substations, with effects lasting up to two hours (Caraballo et al., 2025).

In this work, we present an analysis of the predictive abilities of two GIC models and three $\Delta \mathbf{B}$ models during the May 2024 storm. We also identify empirical relationships between GICs measured at different sites and the relationship between two summary measures, the standard deviation of GIC and $\max|\text{GIC}|$ during the storm and geomagnetic latitude and the β scaling factor (Pulkkinen et al., 2025).

In the remainder of this section, we review the current literature on space weather, GICs, and current methods and approaches to model validation. In section 2, we present a summary of the measurement and prediction data. In section 3, we present the results of the empirical analysis.

1.1 GICs

Geomagnetically induced currents (GICs) are caused by electric currents in Earth’s ionosphere and magnetosphere. Enhancements in these currents are associated with geomagnetic storms and are a direct result of solar activity, such as CMEs (Winter, 2019). These eruptive solar events send outflows of charged particles, along with a release of magnetic energy, driving the magnetospheric-ionospheric response, which leads to current enhancements that result in geoelectric field variations on Earth, driving GICs (Pulkkinen et al., 2017). Extreme events, such as the Carrington Event (Carrington (1859); Blake et al. (2021); Blake et al. (2020); Thomas et al. (2024)), have the potential to produce

GIC more than twice as large as those produced by previously observed Earth-directed extreme events such as the March 1989 storm (Ngwira et al., 2014).

The strength of the geoelectric field, which is the driver of GICs, at a particular point on Earth’s surface depends on latitude and ground conductivity (NERC, 2024b). Higher latitude locations are more likely to experience stronger GICs because they are nearer to the auroral-zone current systems, which tend to be larger and more variable (Winter, 2019). While GICs are generally more intense at high latitudes, they are still present at low to mid latitudes, especially during intense geomagnetic events (Caraballo et al. (2023), Liu et al. (2018)). Global magnetohydrodynamics (MHD) modeling of an extreme geomagnetic events demonstrates a strongly shifted auroral geomagnetic latitude boundary, implying that the region of large induced ground electric fields may be displaced to be nearer the equator, affecting power grids in regions normally far away from the auroral zone, such as southern United States or central/southern Europe (Ngwira et al., 2014). Additionally, locations with more conductive materials in Earth’s crust will experience stronger GICs as currents flow more freely through conductive material (Caraballo et al., 2023).

Particularly large geomagnetic storms can negatively impact terrestrial critical infrastructure, for example, causing radio blackouts (Knipp et al., 2016) and phone system outages (Boteler et al., 1998). GICs, in particular, are known to impact critical infrastructure that relies on long systems of electrical conductors, such as pipelines (Khanal et al., 2019), railway tracks (Boteler (2021); Love et al. (2019)), submarine cables (Boteler et al., 2024), and power transmission networks (Kappenman, 1996). The interaction between infrastructure and GIC can result in damaged equipment, such as transformers (Gaunt & Coetzee, 2007), and even system-wide disturbances, as seen in the 1989 Hydro-Québec blackout (Bolduc, 2002). Extra high-voltage (EHV) transformers in particular are a concern when it comes to the potential catastrophic damage of a geomagnetic storm, as there are $\sim 2,000$ EHV transformers in the United States (MacAlester & Murtagh, 2014). The potential economic impact in the US has been estimated to be a daily loss of GDP ranging from 6.2 to 42 billion dollars U.S. due to power grid failures (Oughton et al., 2017). Given the potential for far-reaching impact on vital infrastructure systems, both accurate prediction and preparation for extreme GIC events are essential.

1.2 Space Weather Strategy

The North American Electric Reliability Corporation (NERC) is an international regulatory body for the United States, Canada, and Mexico whose stated purpose is “to assure the effective and efficient reduction of risks to the reliability and security of the grid” (NERC, 2024a). Among the responsibilities of NERC is developing and enforcing reliability standards for the bulk power system (NERC, 2024a). NERC, under its transmission planning standards, requires analysis of the following categories of contingencies: resulting in a loss of a single element (Category B), resulting in a loss of two or more elements (Category C), and extreme events resulting in two or more elements removed or cascading out of service (Category D) (Chatterjee et al., 2010). According to a NERC report, the two primary risks of the introduction of GIC to the bulk power system are damage to system assets (typically transformers) and loss of reactive power support, leading to voltage instability (Lauby & Rollison, 2012). As such, power systems operators must rely on modeling and prediction capabilities to inform their decision-making.

SWPC has the primary responsibility for monitoring and forecasting solar activity in the United States (Lauby & Rollison, 2012). For geomagnetic storms, SWPC can provide a warning time between 17 and 90 hours before a CME reaches Earth, with larger CMEs taking a shorter time (MacAlester & Murtagh, 2014). However, the magnetic orientation of the associated CME can only be measured by the NASA Advanced Composition Explorer (ACE) and the NOAA Deep Space Climate Observatory (DSCOVR; Burt and Smith (2012)), limiting the advance warning time with known parameters to around 15-20 minutes for a fast-moving CME (MacAlester and Murtagh (2014); Loto’aniu et al. (2022)). Once SWPC issues a warning and/or field GIC sensors are triggered, operating procedures – such as adding more reactive power capability and unloading equipment – are taken at the onset of the event to limit the potential damage (Lauby & Rollison, 2012). Specific examples of these actions are listed by NERC and categorized by warning time as given by SWPC (NERC, 2013a). In addition to real-time preparedness, NERC provides transmission operators with magnetic and thermal transformer models to aid in geomagnetic storm planning (NERC, 2013b).

1.3 Previous Validation Work

Given the various impacts of GICs on critical infrastructure, accurately predicting GICs is vital. As stated in section 1.1, the strength of GICs and their impact on infrastructure at any given location on Earth’s surface depend on several variables, namely latitude, ground conductivity, and grid configuration (Lanabere et al., 2023). In the US, the ground conductivity structure results in more than three orders of magnitude difference in geoelectric hazards (Lucas et al., 2020). Layered 1-D piecewise conductivity models have been demonstrated to be a useful and relatively simple method for describing approximate ground conductivity (e.g., Caraballo et al. (2023), Balch et al. (2023)). These 1-D models, along with latitude and geomagnetic field data, are then used to find the geoelectric field, which is used to compute GIC at geographical points. However, the accuracy of these 1-D models can be limited (Weigel (2017); Caraballo et al. (2023)). 3-D conductivity models, in contrast, are more complex but have been found to better account for deviations in GIC, as they provide a more accurate representation of geologic complexity (Kelbert and Lucas (2020); Alves Ribeiro et al. (2023)). A comparison study of ground electric field calculations using both 1-D and 3-D conductivity models found that, while 3-D conductivity models are more accurate in terms of representing the spatial variation of the peak geoelectric field across a given region, 1-D approximations do still offer an accurate average induction response over the region (Gannon et al., 2017).

Predicting the geomagnetic field is required for predicting GIC. However, current operational global MHD models do not fully capture the ground-level magnetic field variability, which is essential for modeling induction hazards (Haines et al., 2022).

While GIC can impact various essential infrastructure systems, its impact on power grid networks is of particular interest, especially after the Hydro-Quebec outage in March of 1989, which led to a 9-hour blackout and resulted in ~ 13.2 million Canadian dollars in total network damages (Bolduc, 2002). As such, the work of estimating GIC naturally lends itself to estimating its impact on power grid networks. Outside of geographic location, variables such as distance from coastlines, orientation (north-south vs. east-west), operational voltage, and line length can impact the extent of damage caused by GICs (Caraballo et al., 2023). These considerations further complicate the prediction of GIC impacts on power network infrastructure. To accurately estimate substation-level GICs for a given power grid network, surface geoelectric fields must be integrated along power

lines to obtain the line voltage (Kelbert & Lucas, 2020). Such GIC calculations also require location data to estimate the length and orientation of transmission lines in addition to the locations of transformers (Shetye et al., 2018). Additionally, network configuration data is not always available.

To validate such models, calculated GIC values must be compared with GIC measurements. GIC estimates are typically obtained from models localized to a specific nation or region (e.g., Caraballo et al. (2023) in Mexico, Liu et al. (2018) in Ethiopia, and Balch et al. (2023) in the US), as different regions have varying network requirements and available data. The United States alone contains several distinct high-hazard regions: just east of the Appalachian Mountains, in the Upper Midwest, and within the Pacific Northwest (Lucas et al., 2020). This paper will consider GICs in the contiguous US and their effects on the US power grid, particularly in the Tennessee Valley region.

2 Summary of Data

2.1 Measurements

In Figure 1, the solar wind conditions and geomagnetic indices for the event are shown. The modeled and measured GIC and \mathbf{B} used in this work at locations throughout the contiguous United States during the May 2024 storm are summarized in Figure 2. The measured and modeled GIC and TVA $\Delta\mathbf{B}$ data were obtained directly from them; the NERC data were obtained from the NERC ERO data portal, and the data from SWMF, MAGE, and OpenGGCM are described in section 2.4.

Each measured GIC timeseries was inspected for significant errors, such as large gaps or unphysical spikes. Of the 17 TVA and 396 NERC GIC sites, 2 TVA and 355 NERC datasets were removed based on visual inspection. Also, 9 NERC datasets were duplicates of existing TVA-provided data. As a result, in this work, we consider data from 47 GIC sites. In Figure 3, the measured GIC for the 15 TVA sites is shown. In Figure 4, data from NERC’s ERO portal not found in TVA’s data set are shown.

2.2 Transmission Lines

Transmission line geographic and voltage information from the US Department of Homeland Security’s Homeland Infrastructure Foundation-Level Data (HIFLD).

2.3 GIC Estimation

2.3.1 TVA Calculation

One-minute cadence $\mathbf{B}(t)$ measurements USGS-NRCAN magnetometers and the four named TVA magnetometers in Figure 2 were used to compute the parameters of a Spherical Elementary Current System (SECS) model (Amm (1998); Vanhamäki and Juusola (2019)). The SECS model currents were then used to compute $\Delta\mathbf{B}(t)$ at the locations where magnetotelluric transfer (MT) functions are available from the US MT survey sites in the USArray/IRIS data portal (Schultz et al. (2018); Retrieved from the Earth-Scope database). At these sites, the MT transfer functions (Incorporated Research Institutions for Seismology (2011); Kelbert et al. (2018)) were convolved with the SECS $\Delta\mathbf{B}(t)$ to estimate $\mathbf{E}(t)$ at the MT sites. The $\mathbf{E}(t)$ calculation is done in the time domain using a 1024-minute window and a causal convolution technique (Boteler & Pirjola, 2022). $\mathbf{E}(t)$ was then resampled with bilinear interpolation to a regular grid with a 0.5-degree resolution in latitude and longitude, and this timeseries was used by TVA analysts to predict GIC.

2.3.2 Reference Model Calculation

One-minute cadence $\mathbf{B}(t)$ measurements were used to compute the parameters of a SECS model. The magnetometer site IAGA codes are ALE, BOU, BLC, BRD, BRW, BSL, CBB, CMO, DED, FCC, FRD, FRN, GUA, HON, IQA, MEA, NEW, OTT, RES, SHU, SIT, SJG, STJ, TUC, VIC, and YKC. Similar to the TVA calculations in sect. 2.3.1, the SECS model currents are then used to compute $\Delta\mathbf{B}(t)$ at the locations where magnetotelluric transfer (MT) functions are available from the US MT survey sites in the USArray/IRIS data portal (retrieved in May, 2024). At the MT sites, $\mathbf{E}(t)$ was derived by convolving $\Delta\mathbf{B}(f)$ with the transfer functions in the frequency domain. The frequency-domain geoelectric field, $\mathbf{E}(f)$, was then transformed into the time domain using the discrete Fourier transform to obtain $\mathbf{E}(t)$. The locations of MT sites were graphed into Delaunay triangles, each assigned the derived $\mathbf{E}(t)$ field, and interpolated onto transmission lines. The electric potential was then derived using this information and `bezpy` (Lucas & Rigler, 2023).

This reference model was developed to produce GIC estimates when the detailed configuration and parameters of a power system is not known; the power line geometry

and voltages used are described in section 2.2 and the parameter values from the Horton et al. (2012) benchmark model are adopted to construct a system admittance matrix. To solve for the resulting currents in the power network, the Pirjola et al. (2022) method was used.

2.3.3 Results

In Figure 6, a comparison of the measured GIC with the TVA and reference model predictions at the four sites where TVA model predictions are available (Bull Run, Montgomery, Union, and Widows Creek; see Figure 2). The TVA model predictions are at a 1-minute cadence, so the 1-second measured GIC was averaged using 1-minute non-overlapping windows.

Two metrics were used to assess predictions. The square of the Pearson correlation coefficient, cc^2 and the prediction efficiency (Liemohn et al., 2018), defined as $pe = 1 - \sum_t (GIC_p(t) - GIC_m(t))^2 / \sigma_m^2$, where subscript m is for measured and subscript p is for predicted and t is the index of the 1-minute interval from 2024-05-10T15Z to 2024-05-12T06Z. The prediction efficiency is a skill metric relative to sample climatology (a prediction that is the mean of the measured) and represents the fraction of the variance in the measurements that is predicted; $pe = 0$ means the predictor has the same skill as sample climatology. One advantage over cc is that pe is sensitive to errors in magnitude (Detman, 1997). When the means and variances of the measured and predicted data are equal, the prediction error is uncorrelated with the predictor, and the mean of the prediction error is zero, $pe = cc^2$.

A summary of the prediction results is shown in Table 1 for the four sites shown in Figure 6. At these four sites, both models predict GIC with a non-zero correlation. As expected, the TVA model outperforms the reference model, which used benchmark values for network parameters instead of actual values.

Although the TVA model produces $cc > 0.8$ at all sites, the scatter plots in the right column of Figure 6 show that the model over-predicts $|GIC|$ at Bull Run and under-predicts at Montgomery and Widows Creek.

Site ID	σ [A]	σ_{TVA}	σ_{Ref}	cc_{TVA}^2	cc_{Ref}^2	pe_{TVA}	pe_{Ref}
Bull Run	1.50	2.17	0.84	0.80	0.24	0.50	0.24
Widows Creek	1.94	1.21	0.60	0.67	0.34	0.63	0.27
Montgomery	3.71	1.00	7.74	0.86	0.07	0.43	-3.27
Union	3.75	3.55	4.42	0.67	0.36	0.65	0.03

Table 1: Prediction metrics for TVA and Reference model.

The reference model GIC was also calculated at 39 other GIC measurement sites. Over the 43 GIC sites, the reference model GIC had a correlation coefficient between 0.005 and 0.83 and a prediction efficiency between -254 and 0.53 .

Shetye et al. (2018) computed GIC at five sites with GIC instruments (with locations withheld) in the TVA network using ground magnetic field measurements at Fredricksburg, which is ~ 600 miles from the center of the TVA network. The comparison was made over a two-hour period in June of 2015. They used both 1-D and 3-D ground conductivity impedances to calculate the electric field using this magnetic field, and used this electric field in their power system network model. Although they did not provide summary metrics for the model predictions, visually, the model predictions shown in Figure 6 appear to be significantly better. However, it is not possible to determine whether the difference is due to the model results in Figure 6 using the SECS interpolated magnetic field or advances in network modeling.

2.4 ΔB Models

The MAGE, SWMF, and OpenGGCM predicted $\Delta B_H = \sqrt{(\Delta B_x)^2 + (\Delta B_y)^2}$ was compared to the measured ΔB_H for all 15 NERC magnetometer sites, in addition to the two named TVA sites in Figure 2, Bull Run and Union, that had nearby magnetometers). A representative result is shown in Figure 7. To compute cc and pe, the 1-second cadence ΔB measurements were averaged to 1-minute, which was the cadence of the ΔB model predictions.

Visual comparison of the MAGE and SWMF models to the measured ΔB_H for all 17 unique magnetometer sites where simulation results were available shows a consistent

result of MAGE over-predicting while SWMF under-predicts found in Figure 7. For these magnetometer sites, MAGE had a mean $cc = 0.44 \pm 0.03$ and a mean $pe = -3.5 \pm 0.7$. SWMF had a mean $cc = 0.58 \pm 0.01$ and a mean $pe = -0.682 \pm 0.07$. (The uncertainty is the standard error of the mean.) This is consistent with the results in Pulkkinen et al. (2011), in which the average prediction efficiency of ground magnetic fields from global magnetosphere models computed at 12 northern hemisphere locations was one average less than zero for the four geomagnetic storm events considered.

2.5 β factors

The NERC TPL-007 geomagnetic disturbance standard (NERC, 2020) required that US power system operators assess GIC vulnerability using a benchmark simulated electric field. The simulated electric field is

$$E_x(t) = E_{ox}\alpha(y)\beta_x(x, y)f_x(t)$$

$$E_y(t) = E_{oy}\alpha(y)\beta_y(x, y)f_y(t),$$

where $\mathbf{E}_0 = [E_{0x}, E_{0y}]$ is a 1-in-100-year peak geoelectric field amplitude at a reference location, $\alpha = 0.001e^{0.115L}$ is a geomagnetic latitude (L) scaling factor, $\beta = [\beta_x, \beta_y]$ is scaling factor that depends on the local ground conductivity, and $\mathbf{f} = [f_x, f_y]$ is a reference geomagnetic field time series.

The components of β are estimated as the ratio between the peak geoelectric field modeled using a reference ground conductivity model and the peak geoelectric field computed using the best available local ground conductivity model. In NERC TPL-007, 1-D ground conductivity models were used to compute β ; Pulkkinen et al. (2025) used 2-D ground conductivity models derived from MT measurements at $\sim 5,000$ sites on an approximately 0.5° degree grid in the contiguous U.S. to compute β .

Figure 1: Solar wind conditions from the DSCOVR (Deep Space Climate Observatory) spacecraft and select geomagnetic indices during the May 2024 storm event. The IMF data were used as inputs to the simulation models.

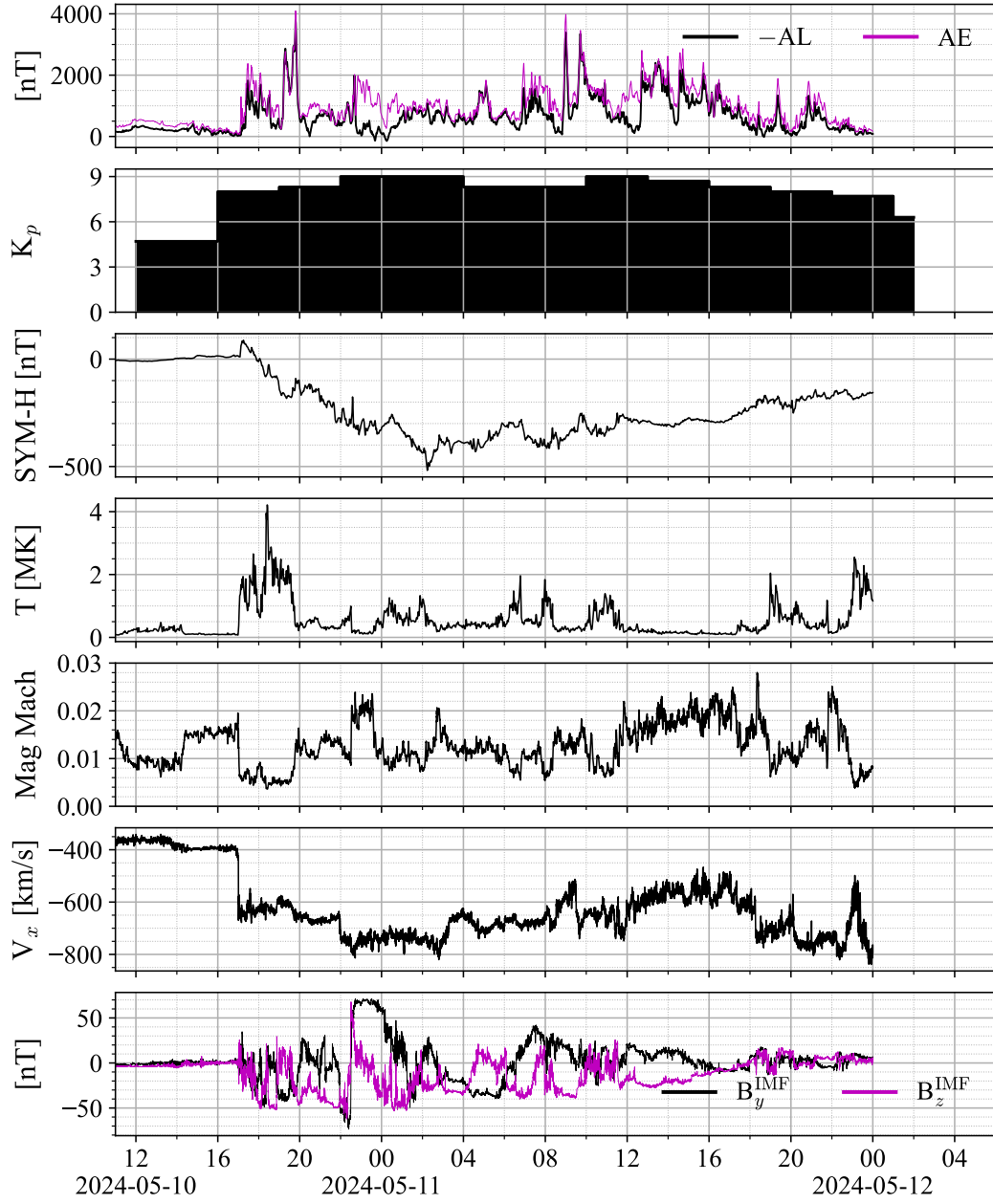


Figure 2: GIC and magnetometer locations and locations where model estimates are available. The approximate TVA operating region is shown in the yellow box.

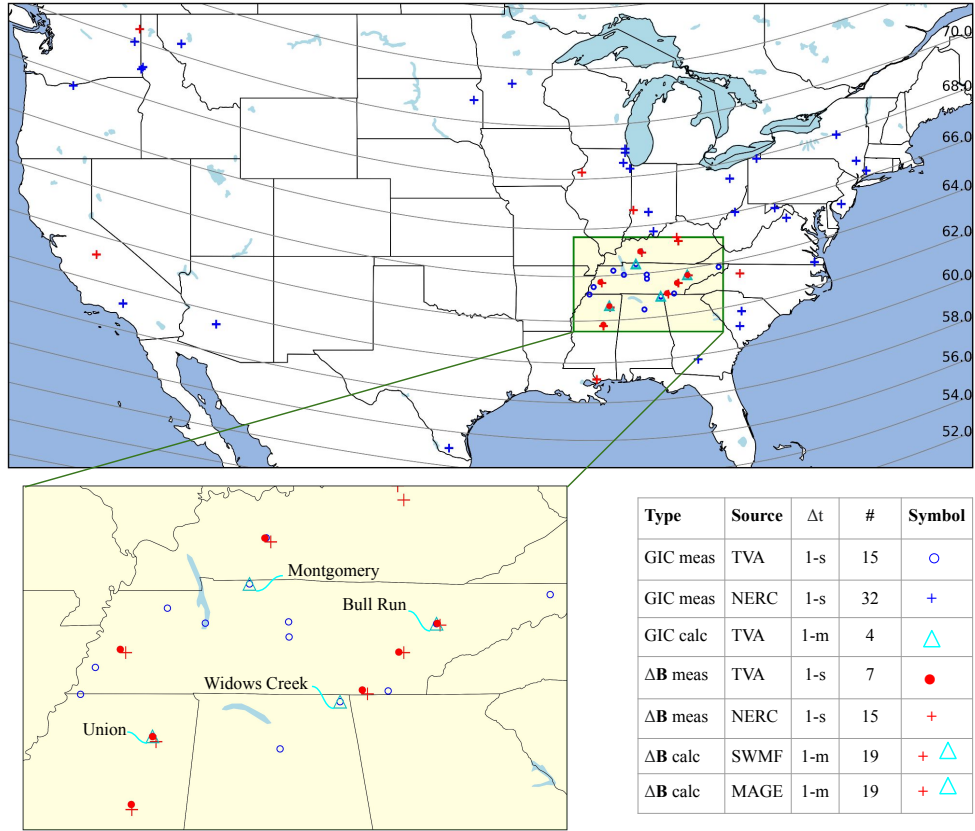


Figure 3: GIC times series from 15 sites from TVA with 40 A baseline offsets sorted by geomagnetic latitude and labeled with the TVA site name and its geomagnetic latitude and longitude in degrees. Data from nine sites also found in the NERC database are indicated with an asterisk.

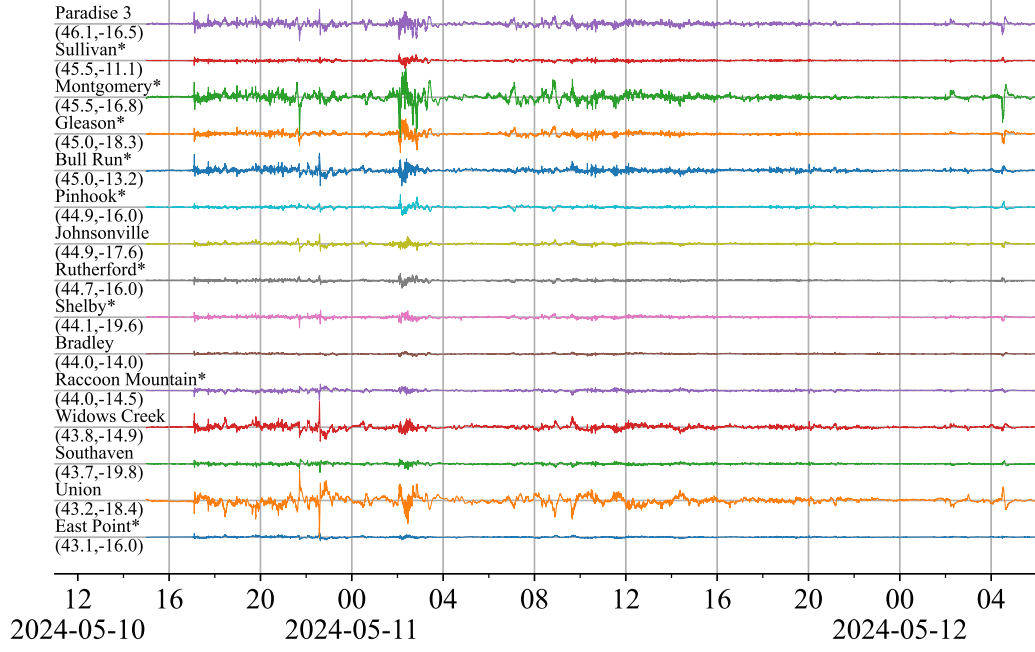


Figure 4: GIC data from 32 sites from NERC's ERO portal with 40 A baseline offsets sorted by geomagnetic latitude and labeled with the NERC site ID and its geomagnetic latitude and longitude in degrees. Data from NERC that were identical to TVA are not shown.

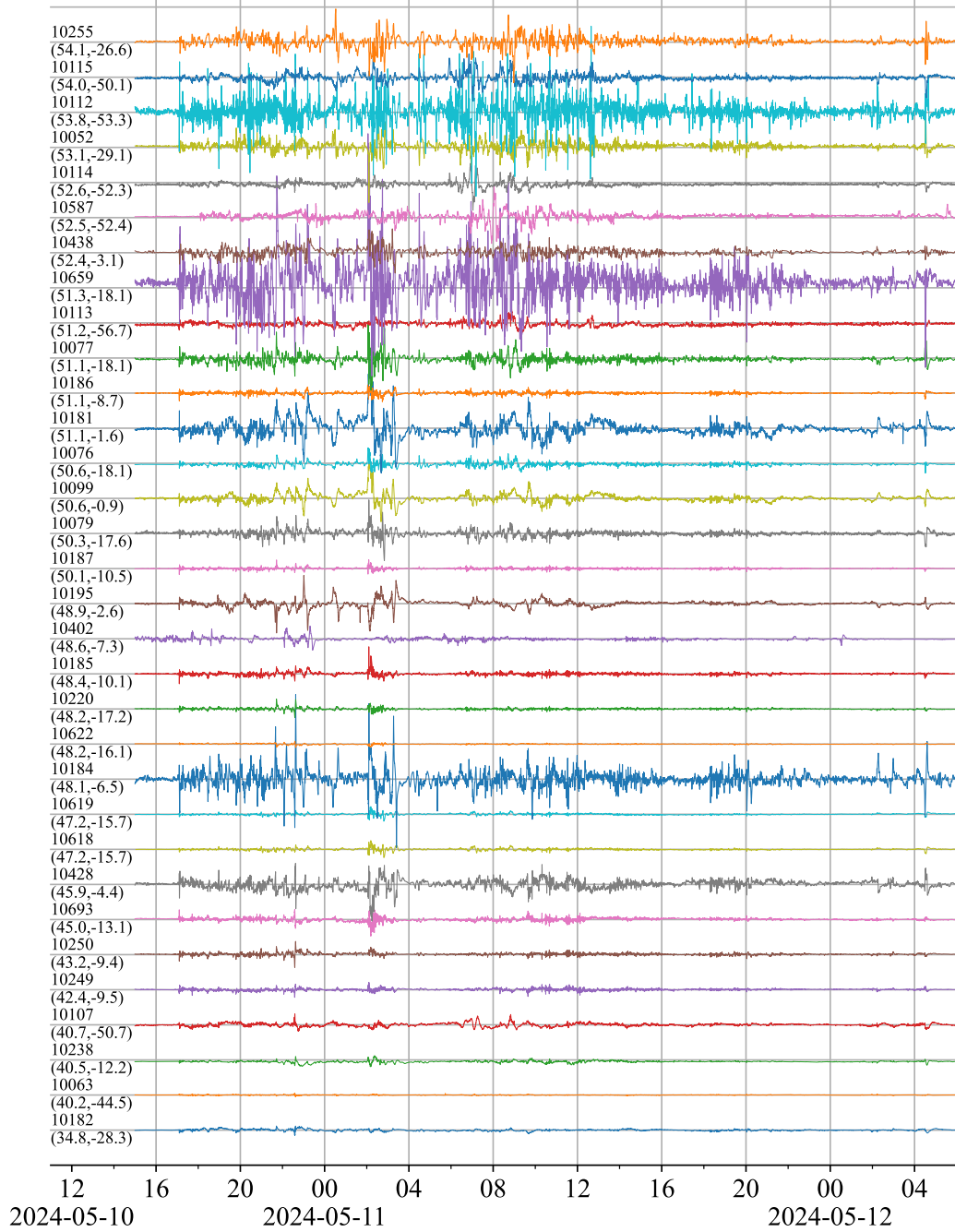
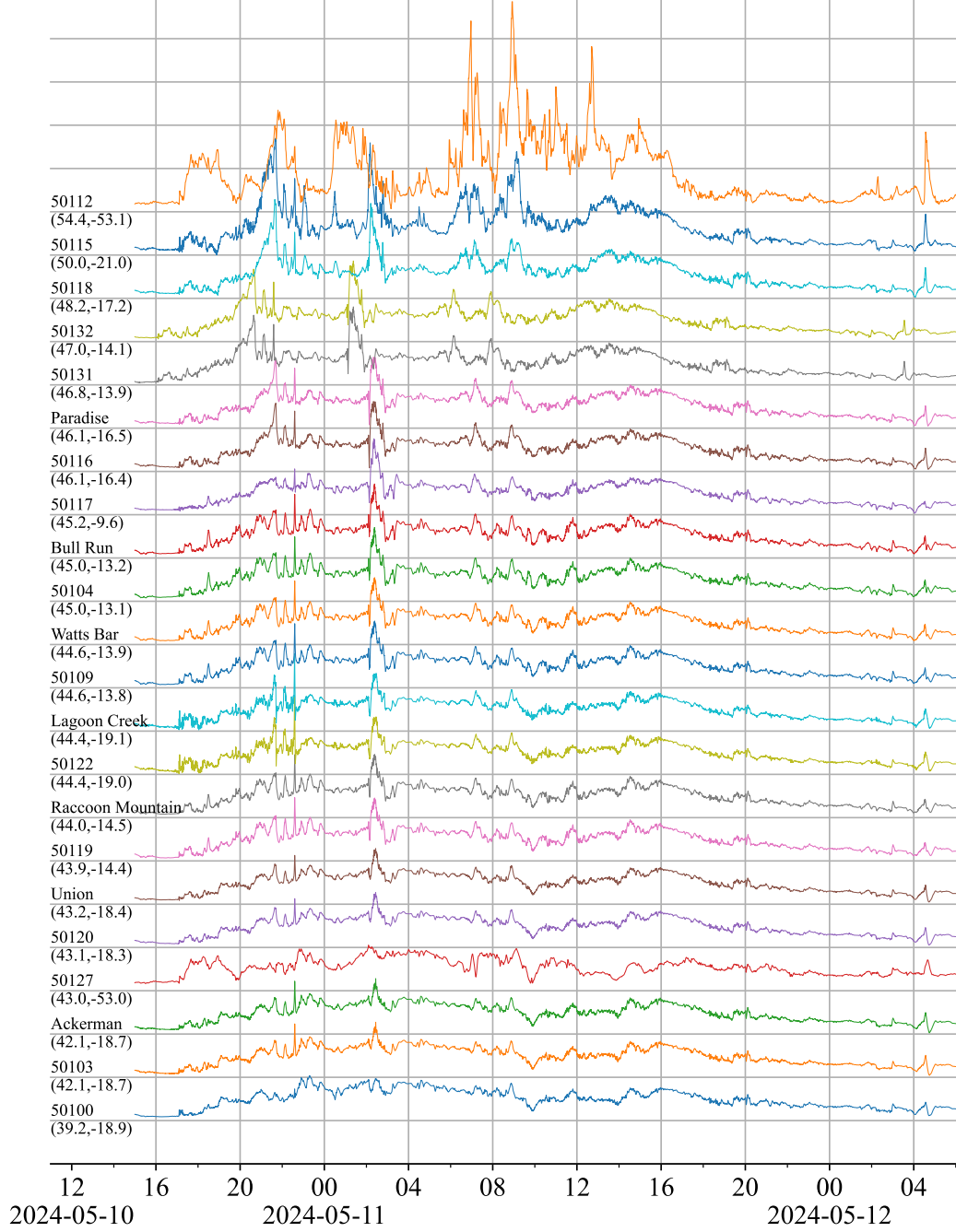


Figure 5: ΔB_H measurements from 15 sites from NERC's ERO portal and 7 sites from TVA with 400 nT baseline offsets sorted by geomagnetic latitude and labeled with the site ID and its geomagnetic latitude and longitude in degrees.



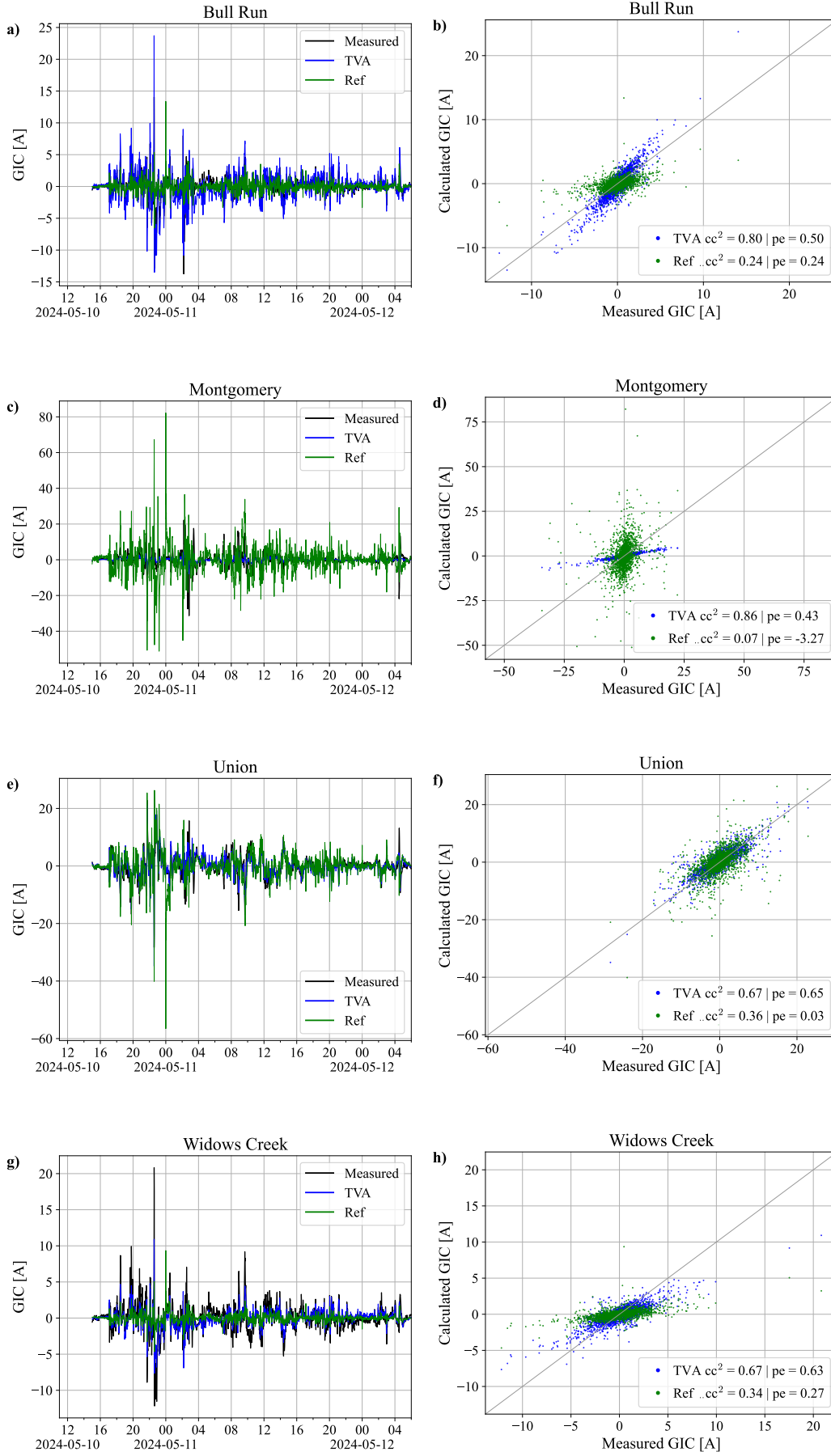


Figure 6: Measured GIC, TVA model, and Reference Model time series.

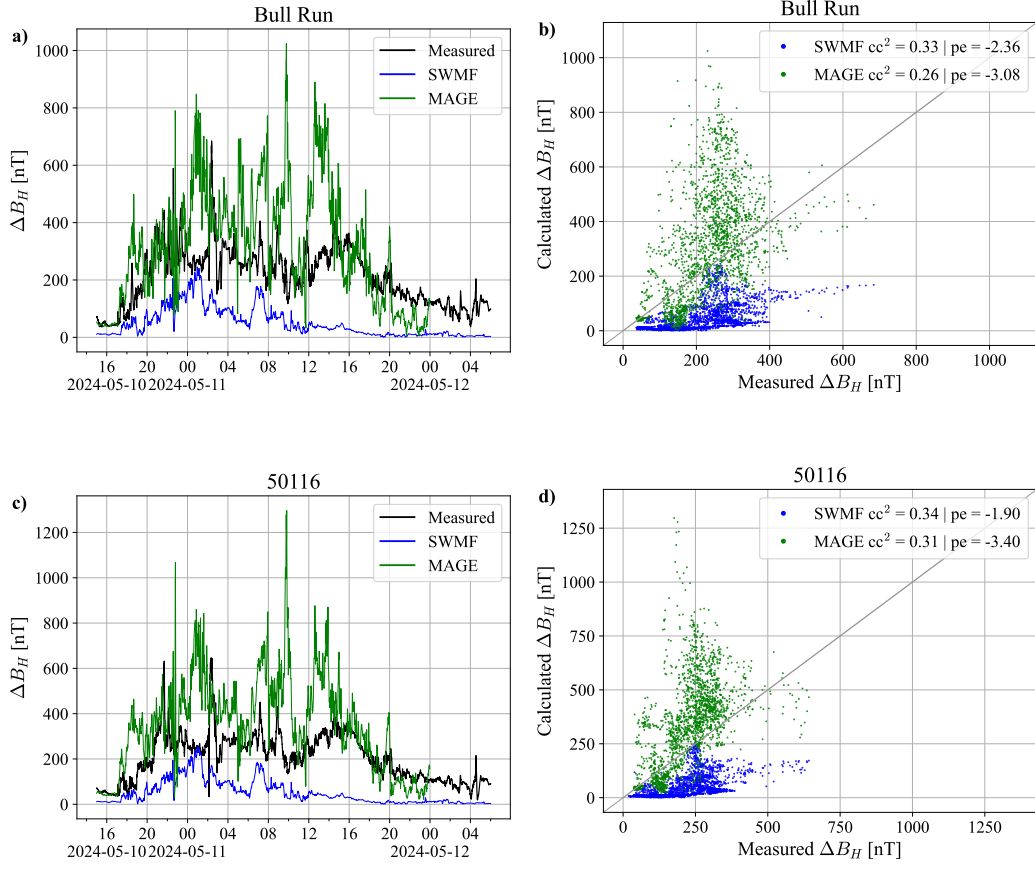


Figure 7: Predicted and measured ΔB_H time series comparison.

3 Empirical Relationships

Ideally, and as in the previous section, GIC would be estimated by convolving $\mathbf{B}(t)$ with a local ground conductivity model to determine $\mathbf{E}(t)$ and using this $\mathbf{E}(t)$ in a network simulation with known parameters. However, real-time measured, or high-quality forecasts of, $\mathbf{B}(t)$ is not always available, and the results of network simulations are not generally available, especially for historical events. As a result, developing empirical relationships that determine how summary measures of GIC at different locations is related can be useful in their absence.

In section 3.1, we consider how GIC at a given site is related to GIC at other sites during the storm. In section 3.2 we consider how $|\text{GIC}_{\text{max}}|$ and the GIC standard deviation at a given site relate to latitude and β .

3.1 Intra-site correlations

In this section, we consider how measured GIC at the 47 sites is related by comparing how the measured GIC relates between the 1,081 unique site pairs. The correlation between each unique site pair was computed. The pair correlations were related to differences in site separation, geomagnetic latitude, $|\beta|$ ($\beta = \sqrt{\beta_x^2 + \beta_y^2}$), the voltage of the power lines on which the GIC monitors were placed, and the number of line connections.

These site pairs varied in separation distance from 0 to 3,957 km. One of the pairs, sites 10619 and 10618, has zero separation distance to the precision of latitude and longitude reported in the metadata (0.1 degree); the next nearest pair has a separation of 5.19 km.

The difference in latitude between site pairs ranged from 0.0° to 21.1° with a mean of 5.2° . The standard deviation of the GIC measured at each of the 47 sites ranged from 0.20 A to 18.0 A with a mean of 2.29 A; the mean standard deviation of site pairs ranged from 0.31 A to 13.4 A. The linearly interpolated β at each site ranged from 0.063 to 3.63. The highest β values were along the eastern coast of the US and in the Great Lakes region, while the lowest were along the Gulf coast. Between the site pairs, the absolute difference in β ranged from 0.0 to 1.57 with a mean of 0.29.

The power line voltage on which the GIC monitors were mounted was estimated by finding the maximum line voltage within a 500 m radius of the latitude and longitude of the GIC monitor. Many transmission did not have a reported voltage. As a result, the voltage difference was only estimated for 325 of the 1,081 site pairs.

The 325 pairs have an absolute voltage difference range of 0 kV to 431 kV with a mean of 152 kV. 43% pairs lie on transmission lines of the same voltage (i.e., $|\Delta V| = 0$ kV).

The results are shown in Figure 8. The correlation between site pairs is weakly dependent on the site pair separation distance (Figure 8a) and the difference in site geographic latitude (Figure 8b). Visually, only a weak relationship exists for differences in β (Figure 8c) and there is no relationship for the differences in nearest power line voltages (Figure 8d).

Similar calculations were performed for the differences in the number of line connections and the mean standard deviation, both of which showed no relationship. In addition, $\log_{10} \beta$ yielded a relationship similar to β .

From these results, and the results of section 2.3, which showed GIC at four TVA sites is highly correlated with GIC computed using a network model, we confirm that observed GIC is highly sensitive to network configuration and local ground conductivity. The correlation between waveforms in site pairs separated by less than 10 km (Figure 8a) varies from near zero to near 1.0. Similarly, site pairs with similar ground conductivity (based on only the proxy β). This conclusion could also be anticipated by a comparison of Figures 5, 3, and 4 – although the waveforms of ΔB_H are much more coherent than the GIC waveforms. Given that GIC depends on ΔB_H , network configuration, and local conductivity, this suggests that the latter two dependencies are significant.

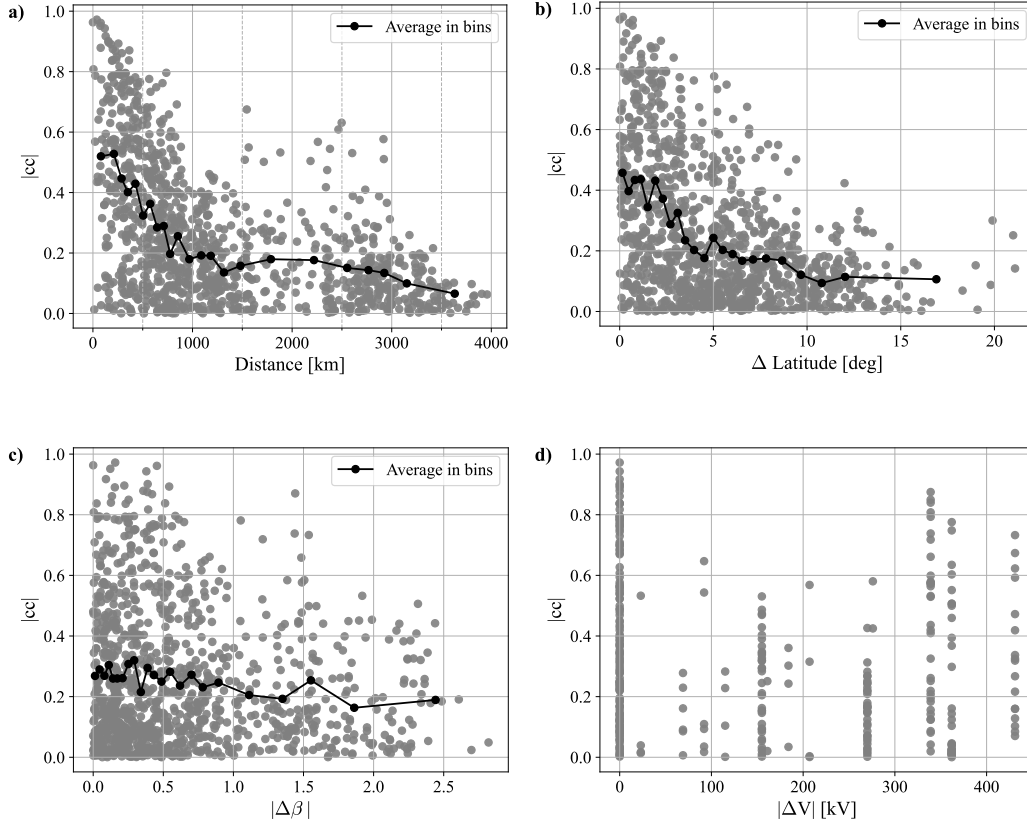


Figure 8: Correlation between GIC time series for 1,081 site pairs vs. differences in site pair distance, latitude, β , and power line voltage nearest to the GIC instrument. The mean $|cc|$ value in 23 bins with 47 points each. ΔV was only available for 325 of the 1,081 site pairs.

3.2 GIC maximum and standard deviation

In the previous section, it was shown that the timeseries of GIC were only weakly correlated between sites, with an average correlation between all pairs of ~ 0.3 . In this section, we consider if the standard deviation during the storm, σ , and maximum GIC magnitude, $|GIC_{\max}|$, and can be estimated using site geomagnetic latitude, λ , and β .

We construct regression models of the form $\sigma = a\lambda + c$ and $\sigma = a\beta + c$ and similar forms for $|GIC_{\max}|$ to determine if geomagnetic latitude and β , can be used to estimate them.

(We used β and $\log_{10} \beta$ in our regression models and found that one with β had a correlation coefficient ~ 0.1 greater than one with $\log_{10} \beta$ for both σ and $|\text{GIC}_{\text{max}}|$. However, the difference in correlation coefficient is not statistically significant.)

In Figure 9a and b, we see that both σ and $|\text{GIC}_{\text{max}}|$ have a moderate linear relationship, with both models having $\text{cc} = 0.54$. Visually, this relationship seems applicable for 44 of the 47 sites because the sites with the four largest values of σ and $|\text{GIC}_{\text{max}}|$ deviate significantly from the regression line.

In Figure 9c and d, we see that β produces similar correlations.

To determine if λ and β have independent information that for predicting σ and $|\text{GIC}_{\text{max}}|$, we compute the 2-D model

$$\sigma = a\lambda + b\beta + c$$

the results of which are shown in Figure 9e and f. The results of all models are given in tables 2 and 3. The difference in the AIC for the 2-D models with the AIC for the 1-D models indicates that the 2-D model is better than either of the 1-D models, statistically.

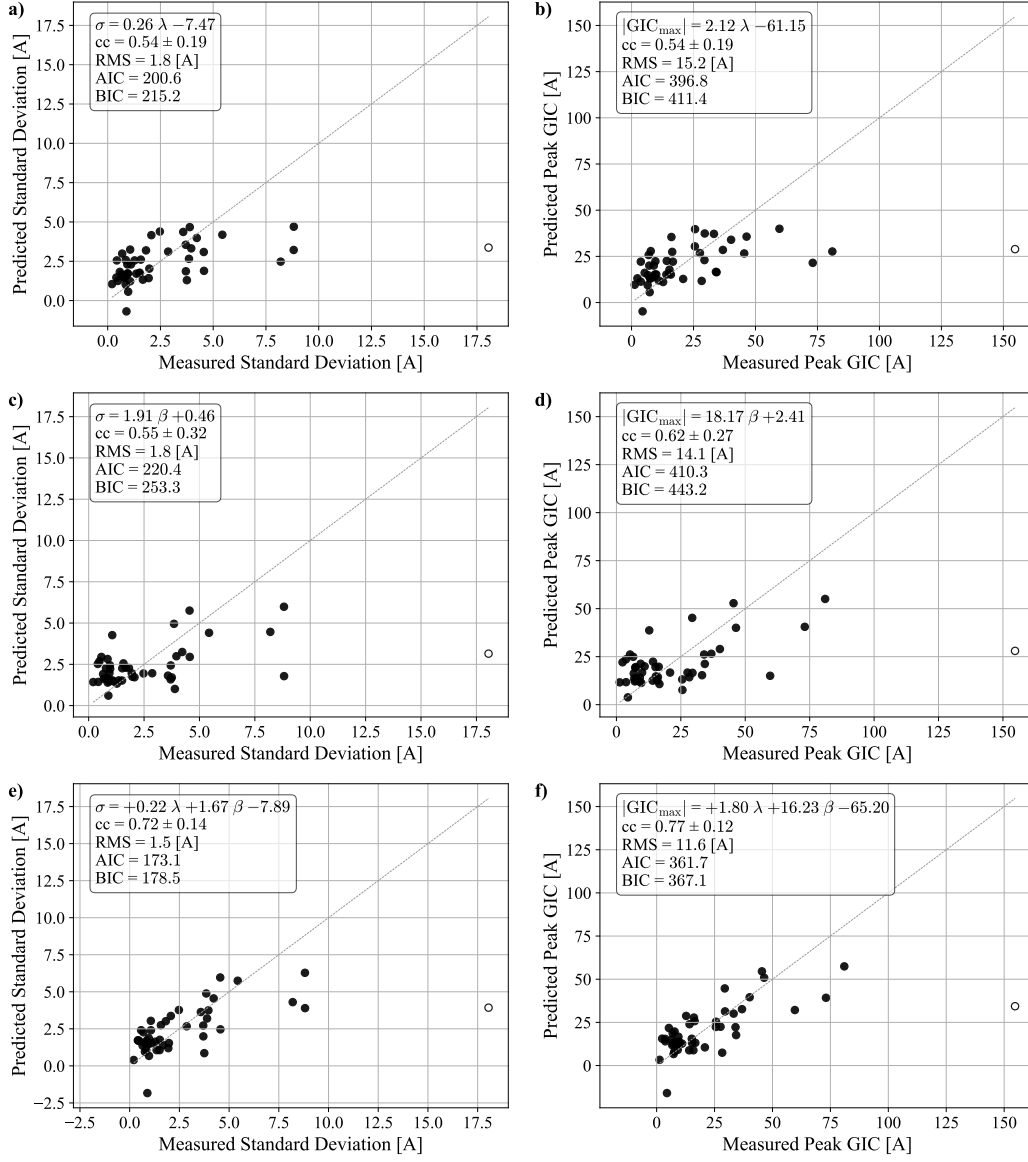


Figure 9: GIC linear regression relationships. The white circle is an outlier that was excluded from the calculation of model parameters.

Fit Equation	$cc \pm 2SE$	RMS [A]	AIC	BIC
$\sigma = 0.26 \lambda - 7.47$	0.54 ± 0.17	1.80	200.6	215.2
$\sigma = 1.91 \beta + 0.46$	0.55 ± 0.32	1.80	220.4	253.3
$\sigma = +0.22 \lambda + 1.67 \beta - 7.89$	0.72 ± 0.13	1.49	173.1	178.5

Table 2

Fit Equation	$cc \pm 2SE$	RMS [A]	AIC	BIC
$ GIC_{\max} = 2.12 \lambda - 61.15$	0.54 ± 0.18	15.18	396.8	411.4
$ GIC_{\max} = 18.17 \beta + 2.41$	0.62 ± 0.28	14.14	410.3	443.2
$ GIC_{\max} = +1.80 \lambda + 16.23 \beta - 65.20$	0.77 ± 0.12	11.55	361.7	367.1

Table 3

4 Summary and Conclusions

In this work, we have analyzed GIC-related measurements and model predictions and showed that

- GIC predicted using measured ground magnetic fields convolved with a 2-D impedance tensor to produce a local geoelectric field that is used to drive a power system simulation produces predictions of measured GIC with correlations greater than 0.8 and prediction efficiencies in the range of 0.4 to 0.6. A reference model that uses recommended estimates for unknown network parameters and the same geoelectric field gives lower prediction efficiencies, as expected. The difference between the network-computed results and the reference model can be used as a rough estimate of uncertainty when only results from a reference model are available.
- The predictions from global magnetosphere models of ΔB_H are highly model-dependent, and although the model predictions' correlations with ΔB_H are approximately 0.5, the prediction efficiencies are low, indicating that the fraction of the variance of the observed ΔB_H is small. This indicates that if model-predicted ΔB_H were used in place of observed ΔB_H to compute the geoelectric field, the quality of the GIC will be significantly lower than when measured ΔB_H is used.
- Although the $\Delta \mathbf{B}$ time series are coherent across large distances, GIC is not. The GIC time series measured at two nearby sites can vary between 0.05 and 0.95. This result confirms the expectation that power system network geometry and parameters have a significant influence on GIC, even if the local magnetic and electric field is similar between two sites.
- The standard deviation and maximum magnitude of GIC can be estimated using a linear relationship to the measurement site's geomagnetic latitude and β scaling factor. This simple linear relationship can be used for extreme scenario estimation and approximation.

References

- Alves Ribeiro, J., Pinheiro, F. J. G., Pais, M. A., Santos, R., Cardoso, J., Baltazar-Soares, P., & Monteiro Santos, F. A. (2023). Toward More Accurate GIC Estimations in the Portuguese Power Network. *Space Weather*, 21(6), e2022SW003397. doi: <https://doi.org/10.1029/2022SW003397>
- Amm, O. (1998). Method of characteristics in spherical geometry applied to a harang-discontinuity situation. *Annales Geophysicae*, 16(4). doi: 10.1007/s00585-998-0413-2
- Balch, C. C., Jing, C., Kelbert, A., Arons, P., & Richardson, K. (2023). Geoelectric Field Model Validation in the Southern California Edison System: Case Study. In *2023 IEEE Energy Conversion Congress and Exposition (ECCE)* (p. 6107-6114). doi: 10.1109/ECCE53617.2023.10362883
- Blake, S. P., Pulkkinen, A., Schuck, P. W., Gloer, A., Oliveira, D. M., Welling, D. T., ... Quaresima, G. (2021). Recreating the Horizontal Magnetic Field at Colaba During the Carrington Event With Geospace Simulations. *Space Weather*, 19(5). doi: 10.1029/2020sw002585
- Blake, S. P., Pulkkinen, A., Schuck, P. W., Nevanlinna, H., Reale, O., Veenadhari, B., & Mukherjee, S. (2020). Magnetic Field Measurements From Rome During the August–September 1859 Storms. *Journal of Geophysical Research: Space Physics*, 125(6). doi: 10.1029/2019ja027336
- Bolduc, L. (2002). GIC observations and studies in the Hydro-Québec power system. *Journal of Atmospheric and Solar-Terrestrial Physics*, 64(16), 1793–1802. Retrieved from <https://www.sciencedirect.com/science/article/pii/S1364682602001281> doi: [https://doi.org/10.1016/S1364-6826\(02\)00128-1](https://doi.org/10.1016/S1364-6826(02)00128-1)
- Boteler, D. H. (2021). Modeling Geomagnetic Interference on Railway Signaling Track Circuits. *Space Weather*, 19(1), e2020SW002609. doi: <https://doi.org/10.1029/2020SW002609>
- Boteler, D. H., Chakraborty, S., Shi, X., Hartinger, M. D., & Wang, X. (2024). An examination of geomagnetic induction in submarine cables. *Space Weather*, 22(2), e2023SW003687. doi: <https://doi.org/10.1029/2023SW003687>
- Boteler, D. H., & Pirjola, R. J. (2022). Electric field calculations for real-time space weather alerting systems. *Geophysical Journal International*, 230(2), 1181–1196. doi: 10.1093/gji/ggac104

- Boteler, D. H., Pirjola, R. J., & Nevanlinna, H. (1998). The effects of geomagnetic disturbances on electrical systems at the Earth's surface. *Advances in Space Research*, 22(1), 17–27. doi: [https://doi.org/10.1016/S0273-1177\(97\)01096-X](https://doi.org/10.1016/S0273-1177(97)01096-X)
- Burt, J., & Smith, B. (2012). Deep Space Climate Observatory: The DSCOVR mission. In *2012 IEEE Aerospace Conference*. IEEE. doi: 10.1109/aero.2012.6187025
- Caraballo, R., González-Esparza, J. A., Pacheco, C. R., & Corona-Romero, P. (2023). Improved Model for GIC Calculation in the Mexican Power Grid. *Space Weather*, 21(10), e2022SW003202. doi: <https://doi.org/10.1029/2022SW003202>
- Caraballo, R., González-Esparza, J. A., Pacheco, C. R., Corona-Romero, P., Arzate-Flores, J. A., & Castellanos-Velazco, C. I. (2025). The impact of geomagnetically induced currents (gic) on the mexican power grid: Numerical modeling and observations from the 10 may 2024, geomagnetic storm. *Geophysical Research Letters*, 52(4), e2024GL112749. doi: <https://doi.org/10.1029/2024GL112749>
- Carrington, R. C. (1859). Description of a Singular Appearance seen in the Sun on September 1, 1859. *Monthly Notices of the Royal Astronomical Society*, 20(1), 13–15. doi: 10.1093/mnras/20.1.13
- Chatterjee, D., Webb, J., Gao, Q., Vaiman, M. Y., Vaiman, M. M., & Povolotskiy, M. (2010). N-1-1 AC contingency analysis as a part of NERC compliance studies at midwest ISO. In *Ieee pes t&d 2010* (p. 1-7). doi: 10.1109/TDC.2010.5484209
- Detman, T. R. (1997). Toward Real-Time Operational Model Predictions. *Second International Workshop on Artificial Intelligence Applications*.
- Gannon, J. L., Birchfield, A. B., Shetye, K. S., & Overbye, T. J. (2017). A Comparison of Peak Electric Fields and GICs in the Pacific Northwest Using 1-D and 3-D Conductivity. *Space Weather*, 15(11), 1535-1547. doi: <https://doi.org/10.1002/2017SW001677>
- Gaunt, C. T., & Coetzee, G. (2007). Transformer failures in regions incorrectly considered to have low GIC-risk. In *2007 IEEE Lausanne Power Tech* (p. 807-812). doi: 10.1109/PCT.2007.4538419
- Haines, C., Owens, M. J., Barnard, L., Lockwood, M., Beggan, C. D., Thom-

- son, A. W. P., & Rogers, N. C. (2022). Toward gic forecasting: Statistical downscaling of the geomagnetic field to improve geoelectric field forecasts. *Space Weather*, 20(1), e2021SW002903. doi: <https://doi.org/10.1029/2021SW002903>
- Horton, R., Boteler, D., Overbye, T. J., Pirjola, R., & Dugan, R. C. (2012). A Test Case for the Calculation of Geomagnetically Induced Currents. *IEEE Transactions on Power Delivery*, 27(4), 2368–2373. doi: 10.1109/tpwrd.2012.2206407
- Incorporated Research Institutions for Seismology. (2011). *Data services products: Emtf, the magnetotelluric transfer functions*. Incorporated Research Institutions for Seismology. Retrieved from <http://ds.iris.edu/ds/products/emtf> doi: 10.17611/DP/EMTF.1
- Johnson-Groh, M. (2024, 05). *How NASA Tracked the Most Intense Solar Storm in Decades*. NASA’s Goddard Space Flight Center. Retrieved from <https://science.nasa.gov/science-research/heliophysics/how-nasa-tracked-the-most-intense-solar-storm-in-decades/>
- Kappenman, J. (1996). Geomagnetic storms and their impact on power systems. *IEEE Power Engineering Review*, 16(5), 5-. doi: 10.1109/MPER.1996.491910
- Karan, D. K., Martinis, C. R., Daniell, R. E., Eastes, R. W., Wang, W., McClintock, W. E., ... England, S. (2024). GOLD Observations of the Merging of the Southern Crest of the Equatorial Ionization Anomaly and Aurora During the 10 and 11 May 2024 Mother’s Day Super Geomagnetic Storm. *Geophysical Research Letters*, 51(15), e2024GL110632. doi: <https://doi.org/10.1029/2024GL110632>
- Kelbert, A., Erofeeva, S., Trabant, C., Karstens, R., & Van Fossen, M. (2018). Taking magnetotelluric data out of the drawer. *Eos*, 99. doi: 10.1029/2018eo112859
- Kelbert, A., & Lucas, G. M. (2020). Modified GIC Estimation Using 3-D Earth Conductivity. *Space Weather*, 18(8), e2020SW002467. doi: <https://doi.org/10.1029/2020SW002467>
- Khanal, K., Adhikari, B., Chapagain, N. P., & Bhattarai, B. (2019). HILDCAA-Related GIC and Possible Corrosion Hazard in Underground Pipelines: A Comparison Based on Wavelet Transform. *Space Weather*, 17(2), 238-251. doi: <https://doi.org/10.1029/2018SW001879>

- Knipp, D. J., Ramsay, A. C., Beard, E. D., Boright, A. L., Cade, W. B., Hewins, I. M., . . . Smart, D. F. (2016). The May 1967 great storm and radio disruption event: Extreme space weather and extraordinary responses. *Space Weather*, *14*(9), 614-633. doi: <https://doi.org/10.1002/2016SW001423>
- Kruparova, O., Krupar, V., Szabo, A., Lario, D., Nieves-Chinchilla, T., & Martinez Oliveros, J. C. (2024). Unveiling the Interplanetary Solar Radio Bursts of the 2024 Mother’s Day Solar Storm. *The Astrophysical Journal Letters*, *970*(1), L13. doi: 10.3847/2041-8213/ad5da6
- Kwak, Y.-S., Kim, J.-H., Kim, S., Miyashita, Y., Yang, T., Park, S.-H., . . . Talha, M. (2024). Observational Overview of the May 2024 G5-Level Geomagnetic Storm: From Solar Eruptions to Terrestrial Consequences. *Journal of Astronomy and Space Sciences*, *41*(3), 171-194. doi: 10.5140/JASS.2024.41.3.171
- Lanabere, V., Dimmock, A. P., Rosenqvist, L., Juusola, L., Viljanen, A., Johlander, A., & Odelstad, E. (2023). Analysis of the geoelectric field in sweden over solar cycles 23 and 24: Spatial and temporal variability during strong gic events. *Space Weather*, *21*(12).
- Lauby, M. G., & Rollison, E. (2012). Effects of geomagnetic disturbances on the North American bulk power system. *NERC*.
- Liemohn, M. W., McCollough, J. P., Jordanova, V. K., Ngwira, C. M., Morley, S. K., Cid, C., . . . Vasile, R. (2018). Model Evaluation Guidelines for Geomagnetic Index Predictions. *Space Weather*, *16*(12), 2079–2102. Retrieved from <http://dx.doi.org/10.1029/2018SW002067> doi: 10.1029/2018sw002067
- Liu, C., Ganebo, Y. S., Wang, H., & Li, X. (2018). Geomagnetically Induced Currents in Ethiopia Power Grid: Calculation and Analysis. *IEEE Access*, *6*, 64649-64658. doi: 10.1109/ACCESS.2018.2877618
- Loto’aniu, P. T. M., Romich, K., Rowland, W., Codrescu, S., Biesecker, D., Johnson, J., . . . Stevens, M. (2022). Validation of the DSCOVR Spacecraft Mission Space Weather Solar Wind Products. *Space Weather*, *20*(10), e2022SW003085. doi: <https://doi.org/10.1029/2022SW003085>
- Love, J. J., Hayakawa, H., & Cliver, E. W. (2019). Intensity and impact of the new york railroad superstorm of may 1921. *Space Weather*, *17*(8), 1281–1292. doi: 10.1029/2019sw002250
- Lucas, G. M., Love, J. J., Kelbert, A., Bedrosian, P. A., & Rigler, E. J. (2020).

- A 100-year Geoelectric Hazard Analysis for the U.S. High-Voltage Power Grid. *Space Weather*, 18(2), e2019SW002329. doi: <https://doi.org/10.1029/2019SW002329>
- Lucas, G. M., & Rigler, E. (2023). *greglucas/bezpy: Rel: v0.1.1*. Zenodo. doi: 10.5281/ZENODO.3765860
- MacAlester, M. H., & Murtagh, W. (2014). Extreme Space Weather Impact: An Emergency Management Perspective. *Space Weather*, 12(8), 530-537. doi: <https://doi.org/10.1002/2014SW001095>
- Mlynczak, M. G., Hunt, L. A., Nowak, N., Marshall, B. T., & Mertens, C. J. (2024). Global Thermospheric Infrared Response to the Mother’s Day Weekend Extreme Storm of 2024. *Geophysical Research Letters*, 51(15), e2024GL110701. doi: <https://doi.org/10.1029/2024GL110701>
- NERC. (2013a). *Geomagnetic Disturbance Operating Procedure Template - Transmission Operator*. Retrieved from <https://www.nerc.com/comm/PC/GeomagneticDisturbanceTaskForceGMDTF2013/Template.TOP.pdf>
- NERC. (2013b). *Geomagnetic Disturbance Planning Guide*. Retrieved from https://www.nerc.com/comm/PC/Geomagnetic%20Disturbance%20Task%20Force%20GMDTF%202013/GMD%20Planning%20Guide_approved.pdf
- NERC. (2020). *North American Electric Reliability Corporation (2020), TPL-007-3 – Transmission System Planned Performance for Geomagnetic Disturbance Events*. Retrieved from <https://www.nerc.com/pa/Stand/Reliability%20Standards/TPL-007-3.pdf>
- NERC. (2024a). *About nerc*. Retrieved from <https://www.nerc.com/AboutNERC/Pages/default.aspx>
- NERC. (2024b). *North American Electric Reliability Corporation (2024), TPL-007-4 – Transmission System Planned Performance for Geomagnetic Disturbance Events*. Retrieved from <https://www.nerc.com/pa/Stand/Reliability%20Standards/tpl-007-4.PDF>
- Ngwira, C. M., Pulkkinen, A., Kuznetsova, M. M., & Gloer, A. (2014). Modeling extreme “Carrington-type” space weather events using three-dimensional global MHD simulations. *Journal of Geophysical Research: Space Physics*, 119(6), 4456-4474. doi: <https://doi.org/10.1002/2013JA019661>
- Oughton, E. J., Skelton, A., Horne, R. B., Thomson, A. W. P., & Gaunt, C. T.

- (2017). Quantifying the daily economic impact of extreme space weather due to failure in electricity transmission infrastructure. *Space Weather*, 15(1), 65-83. doi: <https://doi.org/10.1002/2016SW001491>
- Parker, W. E., & Linares, R. (2024). Satellite drag analysis during the may 2024 gannon geomagnetic storm. *Journal of Spacecraft and Rockets*, 61(5), 1412-1416. doi: 10.2514/1.A36164
- Pirjola, R. J., Boteler, D. H., Tuck, L., & Marsal, S. (2022). The Lehtinen–Pirjola method modified for efficient modelling of geomagnetically induced currents in multiple voltage levels of a power network. *Annales Geophysicae*, 40(2), 205–215. doi: 10.5194/angeo-40-205-2022
- Pulkkinen, A. A., Bernabeu, E., Thomson, A., Viljanen, A., Pirjola, R., Boteler, D., ... MacAlester, M. (2017). Geomagnetically induced currents: Science, engineering, and applications readiness. *Space Weather*, 15(7), 828-856. doi: <https://doi.org/10.1002/2016SW001501>
- Pulkkinen, A. A., Kuznetsova, M., Ridley, A., Raeder, J., Vapirev, A., Weimer, D., ... Chulaki, A. (2011). Geospace Environment Modeling 2008–2009 Challenge: Ground magnetic field perturbations. *Space Weather*, 9(2). doi: 10.1029/2010sw000600
- Pulkkinen, A. A., Schuck, P., Bernabeu, E., Weigel, R. S., & Arritt, R. (2025). A novel approach for geoelectric field response scaling factors used in geomagnetic storm hazard assessments. *Space Weather*.
- Schultz, A., Egbert, G. D., Kelbert, A., Peery, T., Clote, V., Fry, B., & Erofeeva, S. (2018). *USArray TA Magnetotelluric Transfer Functions*. Retrieved from <https://doi.org/10.17611/DP/EMTF/USARRAY/TA> doi: 10.17611/DP/EMTF/USARRAY/TA
- Shetye, K., Gannon, J., Overbye, T., Kobet, G., Grant, I., & Parsons, M. (2018). Comparison of Measured and Simulated Geomagnetically Induced Currents in TVA using Different Conductivity Structures and Network Parameters. In *CIGRE US National Committee 2018 Grid of the Future Symposium* (p. 807-812). Retrieved from https://cigre-usnc.org/wp-content/uploads/2018/10/1A.2_C4.Shetye-1.pdf
- SWPC. (2024a, 05). G5 Conditions Observed! *Space Weather Prediction Center*. Retrieved from <https://www.swpc.noaa.gov/news/g5-conditions>

- observed
- SWPC. (2024b). Historical Comparison of May 2024 Solar Storms. *Space Weather Prediction Center*. Retrieved from <https://www.swpc.noaa.gov/news/historical-comparison-may-2024-solar-storms>
- Thomas, D., Weigel, R. S., Pulkkinen, A., Schuck, P. W., Welling, D. T., & Ngwira, C. M. (2024). What Drove the Carrington Event? An Analysis of Currents and Geospace Regions. *Journal of Geophysical Research: Space Physics*, 129(7). doi: 10.1029/2024ja032556
- Tulasi Ram, S., Veenadhari, B., Dimri, A. P., Bulusu, J., Bagiya, M., Gurubaran, S., ... Vichare, G. (2024). Super-Intense Geomagnetic Storm on 10–11 May 2024: Possible Mechanisms and Impacts. *Space Weather*, 22(12), e2024SW004126. doi: <https://doi.org/10.1029/2024SW004126>
- Vanhamäki, H., & Juusola, L. (2019). Correction to: Introduction to Spherical Elementary Current Systems. In *Ionospheric Multi-Spacecraft Analysis Tools* (p. C1–C1). Springer International Publishing. doi: 10.1007/978-3-030-26732-2_13
- Weigel, R. S. (2017). A comparison of methods for estimating the geoelectric field. *Space Weather*, 15(2), 430–440. doi: 10.1002/2016sw001504
- Winter, L. M. (2019). Geomagnetically Induced Currents from Extreme Space Weather Events. In *Geomagnetically Induced Currents from the Sun to the Power Grid* (p. 195–203). American Geophysical Union (AGU). doi: <https://doi.org/10.1002/9781119434412.ch11>